

Supplementary Information: Printable, castable, nanocrystalline cellulose-epoxy composites exhibiting hierarchical, nacre-like toughening

Abhinav Rao^a, Thibaut Divoux^{b,c}, Crystal Owens^a, and A. John Hart^a

^a*Department of Mechanical Engineering, Massachusetts Institute of Technology,
Cambridge MA 02139, USA*

^b*MultiScale Material Science for Energy and Environment, UMI 3466 CNRS-MIT, 77
Massachusetts Avenue, Cambridge, Massachusetts 02139, USA*

^c*Department of Civil and Environmental Engineering, Massachusetts Institute of
Technology, Cambridge MA 02139, USA*

1 Direct ink writing

The gels are composed of cellulose nanocrystals (CNCs) and an epoxide oligomer dispersed in an organic solvent, here dimethylformamide (Fig. S1a). This process closely follows the gel formulation described in a previous study.¹ The hydroxyl groups on the CNCs crosslink with the epoxide monomers upon heating, which leads to the formation of a gel.² A stress sweep performed at frequency $f = 1$ Hz on a gel of composition with 12.5% CNCs by mass relative to solvent, placed in a parallel-plate geometry connected to a stress-controlled rheometer (AR-G2, TA Instrument) is reported in Fig. S1b. Note that in the gel, epoxide monomer is dispersed in the solvent in a ratio such that the final mass fraction of CNCs in the composite, is 63% after the solvent is dried. The linear mechanical properties of the gel are dominantly elastic ($G'_0 = 1000$ Pa $\gg G'' = 100$ Pa), and the gel yields beyond a certain critical stress of about $\sigma_c \simeq 100$ Pa.

A commercially available desktop 3D printer Hyrel Engine SR printer (Hyrel 3D, Norcross GA) was modified for direct ink writing of crosslinked CNC composites by replacing the standard syringe extruder with a Nordson HP3 pneumatic syringe extruder (Fig. S1c). The extruded composite gel is pictured in Fig. S1d. The printed bed is heated to 50°C, and the gel is deposited in multiple layers through a nozzle of diameter 0.3 mm. The gel expands slightly upon extrusion, and the thickness of each

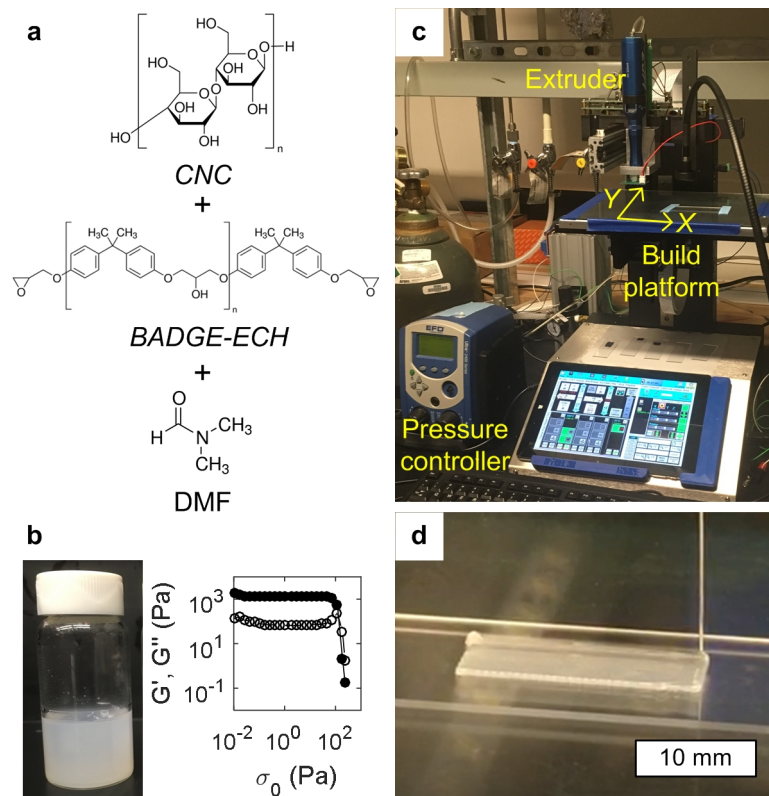


Figure S1: Formulation and direct-write printing of crosslinked CNC composites: a) Chemical formulation of the gel, b) Photograph showing a sample of composite gel with 12.5% wt. CNCs, and a rheological test (stress-sweep at $f = 1$ Hz) illustrating the existence of a yield stress, c) Hyrel 3D printer with a pneumatic extruder and d) Photograph showing an extruded layer during printing onto a glass slide.

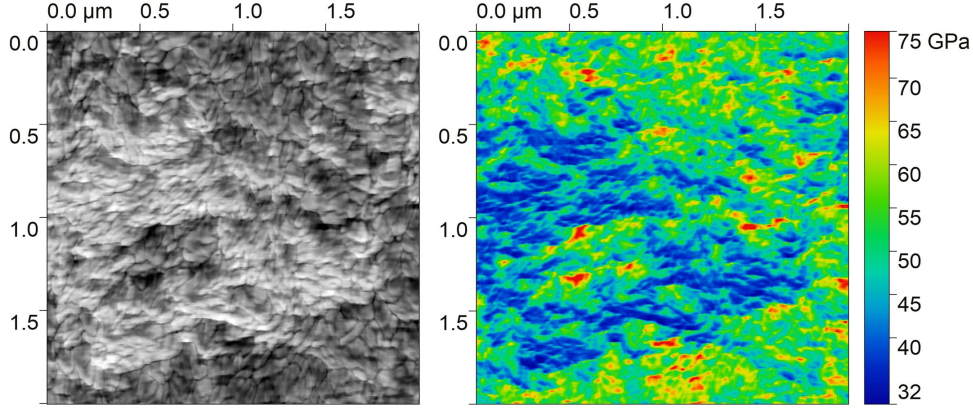


Figure S2: Visualization of grains and modulus map obtained by AMFM imaging

layer is approximately 0.5 mm. UV-curable gels are partially cured under a UV flood lamp (Dymax 2000-EC) for 5 minutes. Following this, they still contain solvent, but have higher mechanical integrity. Aside from this step, the curing process is identical for both UV and thermally curable samples. The sample is then air-dried to remove a majority of the solvent. A two-stage thermal cure - first at 80°C for 6 hours and 130°C for 4 hours is used to fully harden the samples. The printed samples are then polished on a rotary polisher using a silicon carbide polishing paper of grit P4000 (Buehler) prior to any mechanical testing. The thickness of the cured samples was around 1 mm, around 100 times the largest indentation depth.

2 Bimodal atomic force microscopy

In traditional atomic force microscopy (AFM) a cantilever is excited near its resonant frequency, and the amplitude and phase of the cantilever are measured as the tip scans across the sample surface. This information is used to map the topography of the sample using Hertzian mechanics.³ In bimodal AFM, the tip is excited at two separate eigenfrequencies. Amplitude feedback on the first eigenmode is adjusted to maintain a pre-determined set point. This method is used to determine topography information similar to conventional AFM. A frequency feedback loop operates on the second eigenmode to keep it at resonance as the sample is scanned. The measured changes in frequency are then used to calculate an interaction storage modulus and an effective indentation depth.⁴ This method is known as *AMFM imaging*, and provides simultaneous structural and mechanical information at lengths scales smaller than 100 nm, which are inaccessible by other techniques such as nanoindentation and scanning electron microscopy. Fig. S2 shows an AMFM image of the printed

CNC-epoxide composites. Here the modulus map is obtained by first scanning the composite sample, obtaining the modulus with arbitrary units. Then the same tip and cantilever gain and height settings are used to scan a bare silicon wafer. A calibration factor is then calculated assuming a modulus of 130 GPa for silicon,⁵ and is in turn used to determine the modulus values of the CNC composite.

3 Grain size measurement

Automated measurement of grain sizes from binary images is performed using the linear intercept method, according to the ASTM E1382 standard.^{6,7} The measurement process involves plotting evenly spaced lines across the image, and recording the distances between the detected grain boundaries along each line. This measurement is repeated in four directions, 0° , 90° , 45° , 135° . The measurements along each direction are stored in separate variables and finally combined into a single histogram.

Grain size distributions are computed from the AMFM images. Conventionally, a threshold is used to convert the greyscale image into a binary (black and white) image. The grains and grain boundaries have opposite binary values, and can easily be detected. A Gaussian blur is first applied to the raw indentation image, serving as a low-pass filter to reduce noise. However, the grain boundaries in the indentation images, while visible to the eye, have varying greyscale values. A fixed threshold, therefore, would not accurately detect the grain boundaries across the entire image. Rather than using a fixed threshold, the grain boundaries are identified as the local minima of the greyscale values along a given measurement trace. Fig. S3 shows lines along which grain sizes are measured in the 0° and 90° directions. The normalized greyscale values along the blue highlighted trace are plotted in Fig. S3a, showing the local minima (red stars) corresponding to the grain boundaries. This process is repeated for diagonal traces along the 45° and 135° directions. The local minimum method is adaptive to account for variations in the greyscale value of the grain boundaries within a single image. Furthermore, this method does not require any inputs that could cause inconsistencies across multiple images.

Following the ASTM E1382 protocol, the grain boundaries measured along each direction are stored in separate variables and finally combined into a single histogram. Figure S4 shows a probability distribution of the combined dataset for three regions, denoted (a), (b) and (c) of the same sample alongside the corresponding indentation maps. The three regions are distant by about 1 mm from each other. The probability distributions of the grain sizes are well described by a lognormal probability distribution. The fit parameters corresponding to the three regions are given in Table S1. While the mean and median grain sizes are similar in all three regions, we observe that there are a few grains larger than 200 nm in each region.

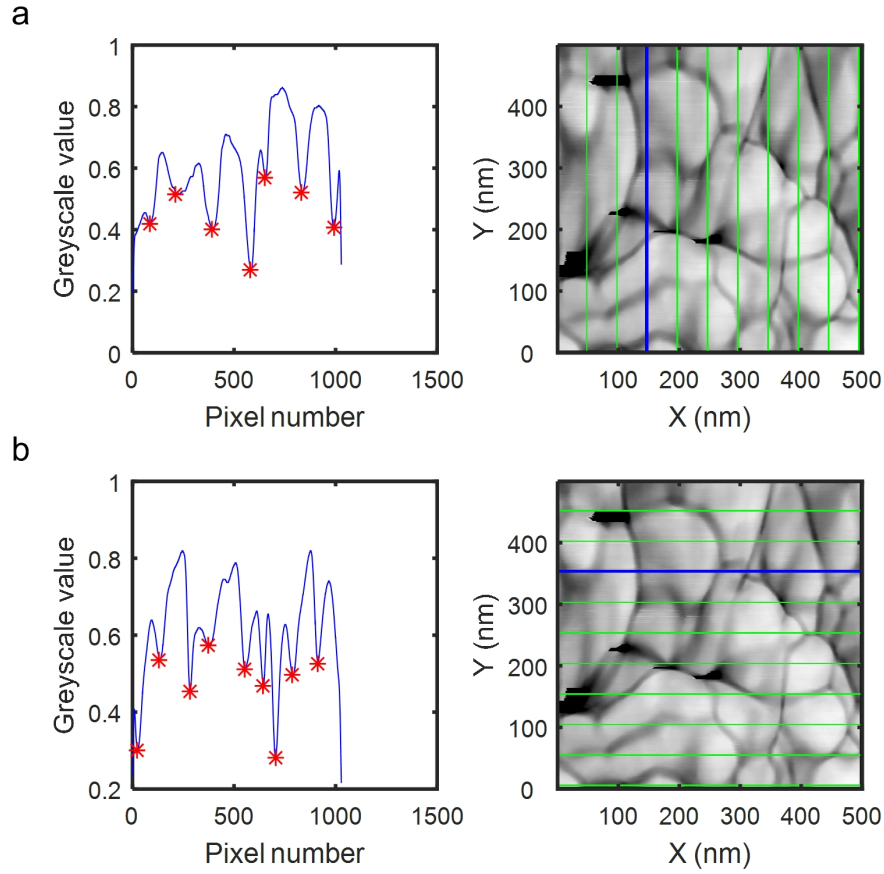


Figure S3: Grain boundary detection along a) horizontal and b) vertical directions. For each data set, the right image correspond to the AMFM data, while the left greyscale profile corresponds to the blue line in the image.

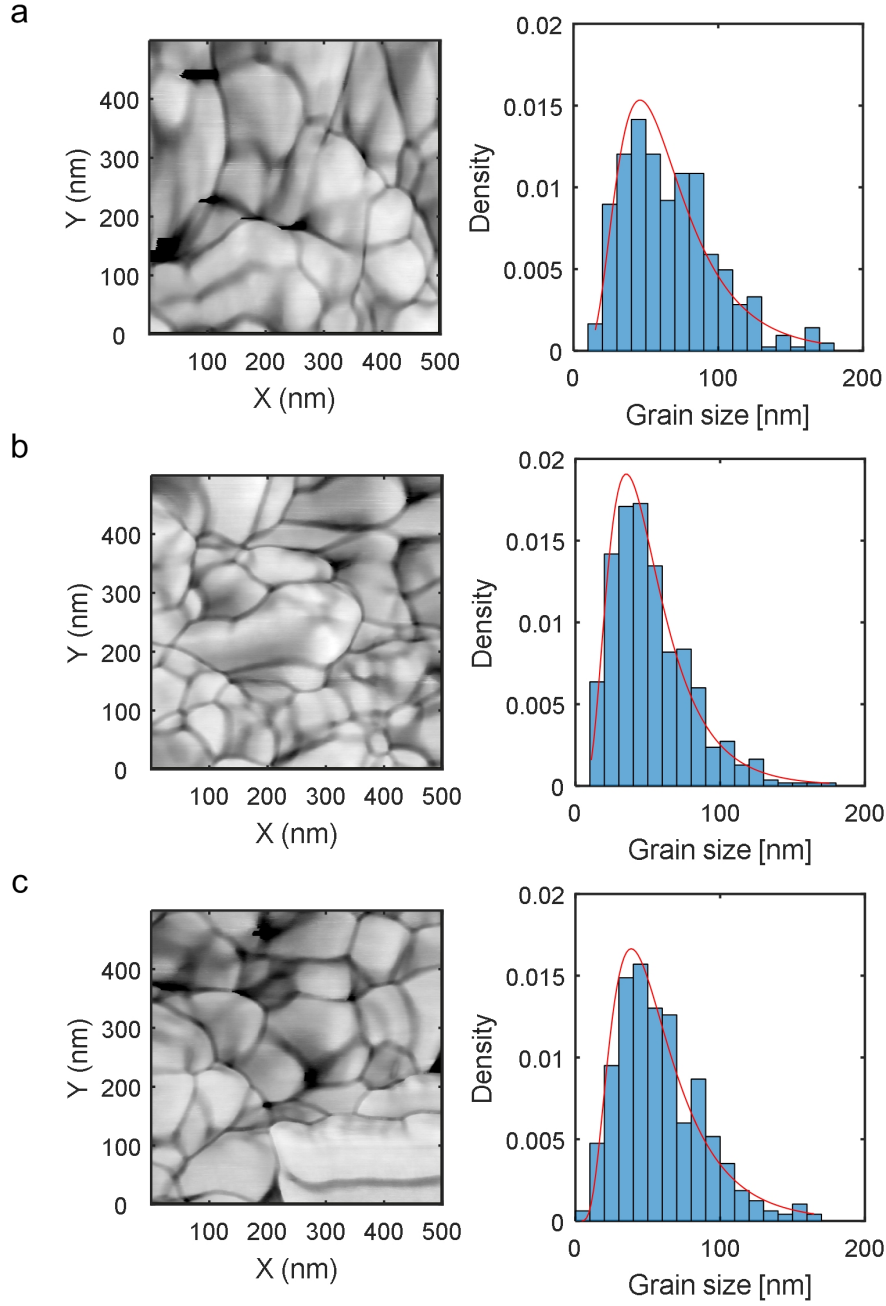


Figure S4: AMFM image (left) and grain size probability distribution (right) at three different locations labelled a, b and c of a CNC-polymer composite sample, with 63% wt. CNCs. The red curves on the probability distribution graphs correspond to the best fit of the data by a lognormal function of parameters listed in Table S1

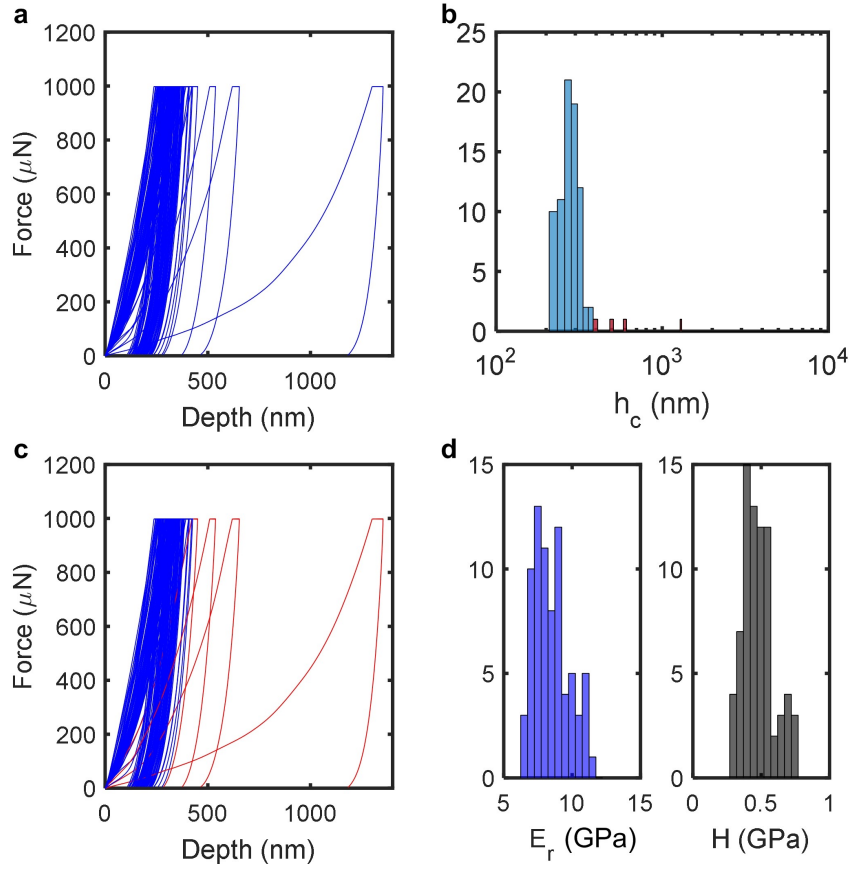


Figure S5: a) Raw data load-displacement (P-H) curves obtained for 81 indents distant by $10\ \mu\text{m}$ performed at a maximum force $1\ \text{mN}$ on a composite with 78% wt. CNCs, b) Histogram of the contact depth h_c showing outliers in red, c) Same P-H curves as in a) where the outliers are highlighted in red, d) Histograms of the indentation modulus E_r and the hardness H without the outliers.

Region	μ	σ	\bar{x} (nm)	M (nm)
a	4.08	0.5	66.81	58.97
b	3.83	0.52	52.69	46.03
c	3.94	0.54	59.48	51.46

Table S1: Lognormal distribution fit parameters for the grain sizes distribution displayed in Figure S4. Data include the scale parameters, μ and σ as well as the mean, \bar{x} and median, M .

4 Detection of outliers in the nanoindentation data

Statistical nanoindentation tests were conducted on a Hysitron Triboindenter equipped with a three-sided pyramid diamond Berkovich indenter. A 3-step trapezoidal load profile is imposed with loading and unloading steps 10 s each, separated by a 5 s hold at peak load. The vertical position of the indenter is recorded simultaneously. Each indent results in a load-displacement (P-H) curve, which is analyzed following the method of Oliver and Pharr to deduce the indentation modulus E_r and the hardness H at the locus of the indent, over a volume which corresponds to 3 to 5 times the maximum indentation depth.⁸ Both systematic and non-systematic errors affect the load-displacement (P-H) curves obtained from a typical nanoindentation experiment. On the one hand, systematic errors are most often attributed to the detection of the contact point between the indenter and the sample surface.⁹ On the other hand, non-systematic errors are due to measurement noise, temperature fluctuations, external disturbances, and material variations.¹⁰

To detect and remove the outliers due to systematic errors, we have devised a simple algorithm. Figure S5a, shows a set of P-H curves obtained from 81 force-controlled indents on a CNC-polymer composite with 72% wt. CNCs. The indents were spaced 10 μm apart, to ensure sufficient separation of the plastic zones, such that each indent can be treated as a separate statistical event. The resulting distribution of contact depth is shown in Figure S5b. The histogram is divided into 25 nm bins, and considering that our samples are relatively homogeneous at the nanoscale, bins with less than two points are considered to be outliers. Using this method, three P-H curves corresponding to the outliers are detected (see red curves in Figure S5c). Finally, the remaining data points are used to calculate the histogram of the indentation modulus and the hardness (Fig. S5d).

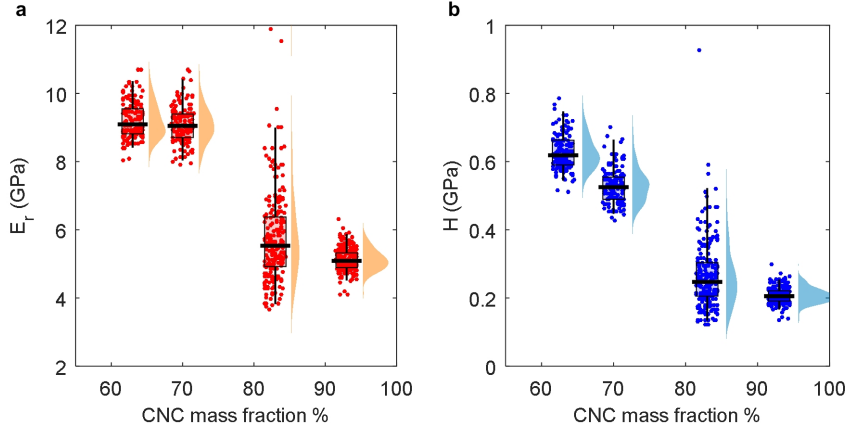


Figure S6: Variation in a) elastic modulus E_r and b) hardness H of printed CNC-epoxide composites with respect to CNC mass fraction.

5 Additional nanoindentation data

Figure S6 shows the elastic modulus and hardness of printed CNC composites with different CNC mass fractions, measured at a peak load of 10 mN. There is no improvement in modulus between a CNC mass fraction of 70% and 63%. Hence the CNC fraction of 63% wt. is chosen as the optimum for further testing.

6 Scratch test

The fracture toughness K_c of the composites are determined from scratch tests performed with a Rockwell indenter connected to a Revetest tester (Anton Paar)¹¹. The vertical load on the indenter was increased linearly from 30 mN to 30 N over a scratch length of 3 mm. Fig. S7 shows the normalized tangential force $F_T / (2pA)^{1/2}$ vs. d/R , where d denotes the depth of the indenter and R its radius (here $R = 200 \mu\text{m}$), measured for a 3 mm long scratch test performed at a velocity of 6 mm/s, with a vertical force that increases from 30 mN to 30 N. For large enough depths, the ratio $F_T / (2pA)^{1/2}$ converges towards a constant value, which is reported as the rate-independent fracture toughness. Here, the CNC-epoxide composite with 63% wt. CNCs has a fracture toughness $K_c = (5.2 \pm 0.2) \text{ MPa.m}^{1/2}$

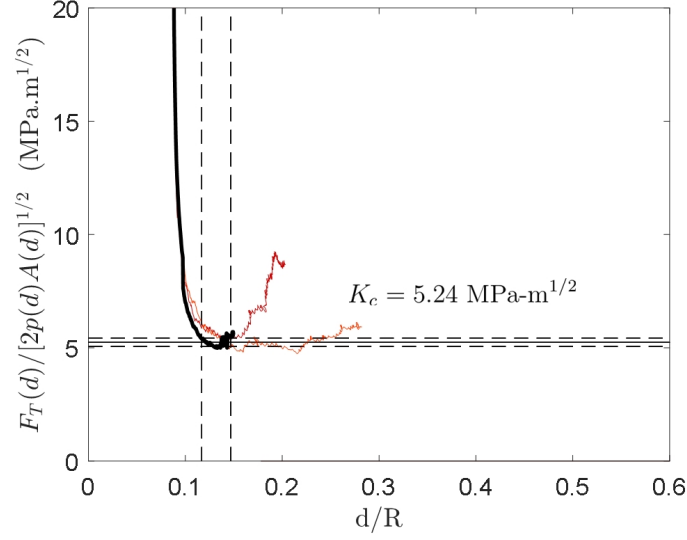


Figure S7: Force versus normalized depth for two scratch tests on 63% wt. CNC/BADGE-ECH composite. Each scratch was performed at a velocity of 6 mm/min, with vertical force increasing from 30 mN to 30 N.

7 Viscoplastic finite element model

In materials with a time-dependent elastic or plastic response, the reduced modulus and hardness obtained by the Oliver-Pharr method, may not sufficiently describe the material.¹⁰ The CNC composites creep during the hold period of the nanoindentation profile, suggesting that a closer investigation of the viscoplastic properties is necessary. Furthermore, the force-displacement curves obtained from nanoindentation contain information about the onset of plastic deformation, not captured by the Oliver-Pharr model-based fit of the unloading curve.¹² Here a finite element model is used to fit the force-depth data obtained from nanoindentation, thereby providing an estimate of the yield stress, Poisson's ratio, strain hardening and viscoplastic flow parameters.

The model is based on an isothermal reduction of the Anand model for large-deformation, isotropic viscoplasticity.^{13,14} The curve used for fitting is selected from the grid to be the one with h_c closest to the mean value of h_c . The following flow equation gives the equivalent plastic strain rate,

$$\dot{\epsilon}^p = \epsilon_0 \left(\frac{\bar{\sigma}}{S} \right)^{1/m} \quad (1)$$

where ϵ_0 is the reference strain rate, $\bar{\sigma}$ is the magnitude of the deviatoric stress and

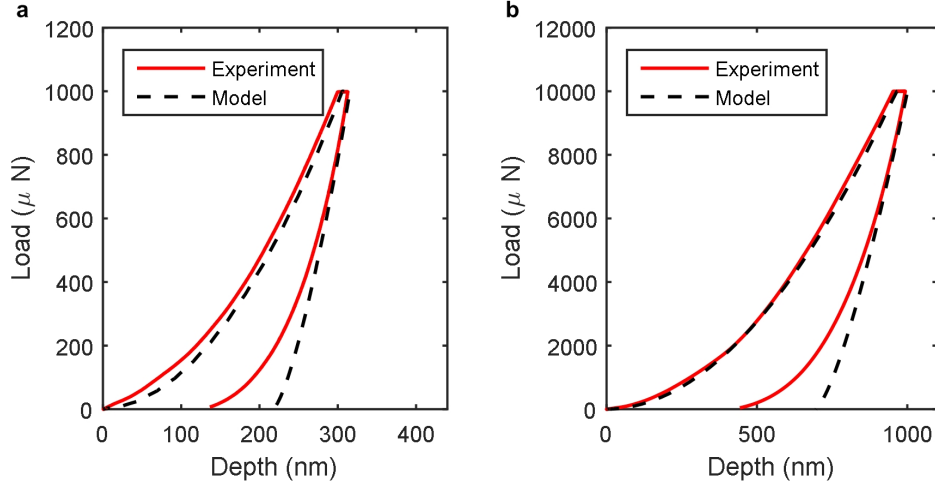


Figure S8: Viscoplastic model fits for the force-depth curves at peak loads of: a) 1 mN and b) 10 mN

m is the rate-sensitivity parameter. The strain-hardening behavior is given by

$$\dot{S} = H_0 \left(1 - \frac{S}{S^*}\right)^a \quad (2)$$

where S is the Piola stress, H_0 , S^* and a are strain-hardening parameters, and S^* represents the saturation value of S .

Parameter	$P_{max} = 1 \text{ mN}$	$P_{max} = 10 \text{ mN}$
Loading rate	0.1 mN/s	1 mN/s
$\dot{\epsilon}_0$	0.12	0.10
m	0.06	0.04

Table S2: Fit parameters describing rate-dependence for indents performed at peak loads of 1 mN and 10 mN with loading rates 0.1 mN/s and 1 mN/s respectively.

The force-depth curve corresponding to the mean plastic deformation, h_c , is selected from each distribution for fitting. Fig. S8 shows the force-depth curves from experiment and the finite element model. The model and experimental data show good agreement for the loading segment and the upper 60% of the unloading segment. The final plastic deformation is not accurately predicted due to difficulties in capturing the contact between the indenter and the sample surface. The Young's modulus and Poisson's ratio obtained from the fit are $E = 8.5 \text{ GPa}$ and $\nu = 0.2$ respectively. The yield strength from the fit, $\sigma_y = 150 \text{ MPa}$. These fit parameters are used for

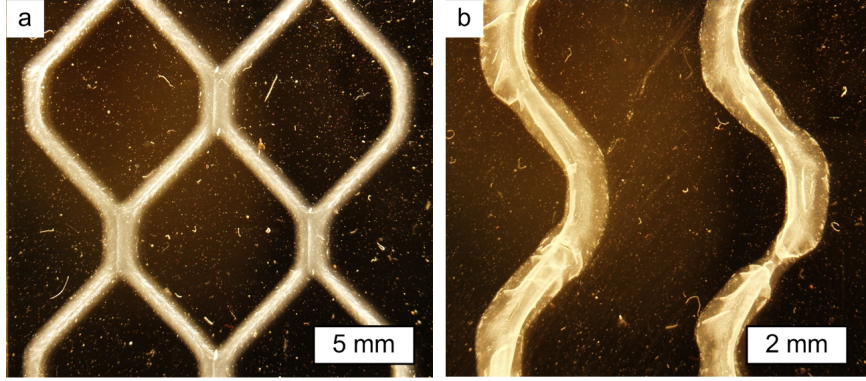


Figure S9: Transmission optical microscopy performed between crossed polarizers of cured printed traces with 63% wt. CNCs by mass: a) honeycomb pattern, b) curvilinear patterns.

both values of P_{max} . However, the loading rates for each dataset are different since the indents were performed with the same loading profile, consisting of 10 s loading and unloading segments, separated by a 5 s hold. Thus, small changes are observed in the parameters that describe the rate-dependence of plastic deformation. Table S2 lists the reference strain rate, and rate-sensitivity parameters for each of the fits.

8 Polarized microscopy

Hardened composites display an anisotropic microstructure as a result of the printing process. Images of 3D printed hardened composites (Fig. S9) were performed between crossed polarizers with a stereo-microscope (Olympus SZX16). The photos reveal a brighter inner section, with a duller outer section. The inner part corresponds to a region of the gel that is not fluidized during the printing phase and thus retains its alignment better. In the outer region, the hydrogen bonds are broken locally as the shear stress is the highest at the walls. Defects due to voids in the extruder are also visible.

References

- [1] A. Rao, T. Divoux, G. H. McKinley, and A. J. Hart, “Shear melting and recovery of crosslinkable cellulose nanocrystal–polymer gels,” *Soft Matter*, vol. 15, no. 21, pp. 4401–4412, 2019.
- [2] F. Khelifa, Y. Habibi, L. Bonnaud, and P. Dubois, “Epoxy Monomers Cured by High Cellulosic Nanocrystal Loading,” *ACS Applied Materials & Interfaces*, vol. 8, pp. 10535–10544, 4 2016.
- [3] A. Labuda, M. Kocun, W. Meinhold, D. Walters, and R. Proksch, “Generalized Hertz model for bimodal nanomechanical mapping,” *Beilstein Journal of Nanotechnology*, vol. 7, pp. 970–982, 7 2016.
- [4] M. Kocun, A. Labuda, W. Meinhold, I. Revenko, and R. Proksch, “Fast, High Resolution, and Wide Modulus Range Nanomechanical Mapping with Bimodal Tapping Mode,” *ACS Nano*, vol. 11, pp. 10097–10105, 10 2017.
- [5] M. A. Hopcroft, W. D. Nix, and T. W. Kenny, “What is the Young’s Modulus of Silicon?,” *Journal of Microelectromechanical Systems*, vol. 19, pp. 229–238, 4 2010.
- [6] P. Lehto, H. Remes, T. Saukkonen, H. Hänninen, and J. Romanoff, “Influence of grain size distribution on the Hall–Petch relationship of welded structural steel,” *Materials Science and Engineering: A*, vol. 592, pp. 28–39, 1 2014.
- [7] ASTM E1382 - 97, “Standard Test Methods for Determining Average Grain Size Using Semiautomatic and Standard test methods for determining average grain size using semiautomatic and automatic image analysis,” 2004.
- [8] W. C. Oliver and G. M. Pharr, “An improved technique for determining hardness and elastic modulus using load and displacement sensing indentation experiments,” *Journal of Materials Research*, vol. 7, pp. 1564–1583, 6 1992.
- [9] Y. Xia, M. Bigerelle, J. Marteau, P.-E. Mazeran, S. Bouvier, and A. Iost, “Effect of surface roughness in the determination of the mechanical properties of material using nanoindentation test,” *Scanning*, vol. 36, pp. 134–149, 1 2014.
- [10] J. Menk, “Uncertainties and Errors in Nanoindentation,” in *Nanoindentation in Materials Science*, InTech, 10 2012.
- [11] A.-T. Akono, P. M. Reis, and F.-J. Ulm, “Scratching as a Fracture Process: From Butter to Steel,” *Physical Review Letters*, vol. 106, p. 204302, 5 2011.

- [12] “Factors Affecting Nanoindentation Test Data BT - Introduction to Contact Mechanics,” pp. 61–82, New York, NY: Springer New York, 2000.
- [13] S. Narayan and L. Anand, “A large deformation elastic–viscoplastic model for lithium,” *Extreme Mechanics Letters*, vol. 24, pp. 21–29, 10 2018.
- [14] G. Z. Wang, Z. N. Cheng, K. Becker, and J. Wilde, “Applying Anand Model to Represent the Viscoplastic Deformation Behavior of Solder Alloys,” *Journal of Electronic Packaging*, vol. 123, no. 3, p. 247, 2001.